Multistatic GNSS-based passive radar for maritime surveillance with long integration times: experimental results

Fabrizio Santi, Federica Pieralice, Debora Pastina
Department of Information Engineering, Electronics and Telecommunications, Sapienza University of Rome
Via Eudossiana, 18 – 00184 – Rome, Italy
santi@diet.uniroma1.it, federica.pieralice@uniroma1.it, debora.pastina@uniroma1.it

***Abstract*—The focus of this paper is on multi-transmitter GNSS passive radar for maritime surveillance. Particularly, working in the range-Doppler domain, the possibility to integrate over long time intervals (required to counteract restricted power budget provided by navigation satellites) the returns from a moving target illuminated by multiple GNSS transmitters is experimentally demonstrated. The obtained results show that the exploitation of multiple satellites can provide an improvement in the detection performance potentially enabling the detection of targets not detectable with the single satellites at the same time allowing target localization.**

Keywords—Passive radar, GNSS-based passive radar, multistatic passive radar, maritime surveillance

I. Introduction

Since many years, the alternative utilization of Global Navigation Satellite Systems (GNSS) has been the focus of an increasing research activity. In the field of radar technology, navigation satellites have been largely investigated as opportunistic sources for passive synthetic aperture radar imagery for permanent area monitoring anywhere in the world [1,2]. Furthermore, GNSS-based passive radar have been investigated for air traffic monitoring applications [3,4]. More recently, GNSS have been considered as opportunistic sources for passive radar systems dedicated to the maritime surveillance. In this framework, the exploitation of GNSS is a prospective solution: the global, reliable and persistent nature of these sources makes them potentially able to guarantee the permanent monitoring of both coastal and open sea areas. In [5], it has been proved that a GNSS-based bistatic radar is fundamentally able to detect vessels at sea, thus opening the way toward new investigations to fully exploit the potential of this technology.

The fundamental bottleneck of the system is represented by the low power budget provided by the navigation satellites, with a power density near the Earth' surface down to -135 dBW/m^2. Thus, high radar cross section (RCS) ships at relatively short stand-offs can be detected by means of straightforward, conventional MTI algorithms, whereas medium/low RCS targets at longer ranges requires to resort to innovative detection techniques. In particular, long integration time MTI techniques have been proposed in [6] and [7], showing that integration times in the order of tens of seconds can be needed to collect signal power enough for ship target detection.

The works in [5-7] addressed the detection problem when a single satellite is exploited. However, one of the main benefits of considering GNSS is the high availability offered by these systems. Typically, around eight satellites are in visibility from each point over the Earth's surface for one completely lunched constellation; therefore, potentially up to 32 satellites may illuminate the same areas when all GPS, GLONASS, Galileo and BeiDou constellations are in full capacity. Because the signals transmitted by different satellites can be recorded by a single GNSS receiver, the GNSS-based passive radar is inherently a multistatic radar system, able to overcome some of the limitations suffered by the bistatic configuration, such as the coarse range resolution [8].

A well-known improvement arising from the exploitation of multiple bistatic couples is the possibility to localize the detected target by means of multilateration. In [9], localization algorithm has been applied to maritime experimental data involving a large ferry and two Galileo satellites. Specifically, the bistatic ranges pertaining the two satellites have been combined by means of the spherical intersection method [10] to provide the target Cartesian track. Nevertheless, such an approach strictly requires that the target can be revealed at the individual bistatic level. That is to say, the localization problem shall be conditional to the detection of a target in the bistatic scenario where, as aforementioned, the power budget can be very unfavorable.

Detectability improvement requires integration. In [6,7], the signal powers are properly added over temporal windows that could be as long as one minute, enabling the detection of targets otherwise inhibited with conventional (i.e., short integration time) approaches. Another source of improvement of power budget can arise from the proper integration over the transmitter's space. In [11], these authors proposed a technique to exploit jointly the signals received by a single receiver during long dwells and over multiple bistatic links. The preliminary analysis provided involving GPS transmitters in a simulated scenario showed that the multi-transmitter long integration time technique is effective in increasing the detection performance of the system with respect to, in turn, the conventional MTI approaches and the single transmitter MTI techniques. Moreover, the spatial diversity can be also exploited to provide the localization of the targets. Namely, the proposed multi-transmitter technique can jointly detect and localize targets not detectable in the bistatic case.

This paper provides an experimental validation of the long integration time multi-transmitter detection technique. The technique has been applied against experimental data considering Galileo satellites and targets belonging to different class types. It will be shown that the long integration time can be a mandatory condition to detect ship targets by means of the GNSS-based passive radar system. Moreover, it will be shown that the exploitation of multiple satellites can jointly provide improvement in the detection performance potentially enabling the detection of targets not detectable with the single satellites and the estimation of their direction-of-arrival (DOA).

The paper is organized as follows. An overview of the GNSS-based multistatic passive radar for maritime surveillance is provided in Section II with a description of the multistatic detection technique. The experimental campaign and the achieved results are provided in Section III while Section IV closes the paper.

II. GNSS-BASED MULTISTATIC RADAR

A. Operative conditions

The considered system comprises GNSS satellites as transmitting sources and a receive-only device (mounted on the coast or on a sea buoy) equipped with two channels: the reference channel, recording the direct satellite signals, and the surveillance channel, collecting the reflections from the surveyed area. Since GNSS operate with frequency or code division approaches, the receiver is able to separate the signals pertaining to the different satellites. Fig. 1 shows the assumed local (O, X, Y, Z) reference system centered in the receiver position and with the x-axis representing the steering direction of the surveillance antenna.

The instantaneous distance among the i-th (i=1,…, N_{Tx}) transmitter (TX), receiver (RX) and target (TG) are defined as follows: $R_{Tx_i-Tg}(t)$ is the i-th TX to TG distance, $R_{Tg-Rx}(t)$ is the TG to RX distance and $R_{Tx_i-Rx}(t)$ is the i-th TX to RX baseline, where t is slow time defined in the interval $[-T/2, T/2]$ being T the overall integration time. The TX and TG positions are also defined by the following angles: ϕ_{Tx_i} is the clockwise angle between x-axis and the satellite projection on x-y plane, θ_{Tx_i} is the out-of-plane angle between the x-y plane and the satellite, ϕ_{Tg} is the clockwise angle between x-axis and target direction (i.e., the target DOA).

Accounting for a compensation of the instantaneous baseline, the bistatic target range is defined as

$$r_i(t) = R_{Tx_i-Tg}(t) + R_{Tg-Rx}(t) - R_{Tx_i-Rx}(t) \quad (1)$$

and bistatic target Doppler frequency is

$$f_i(t) = -\frac{1}{\lambda}\dot{r}_i(t) \quad (2)$$

being λ the wavelength of the transmitted signal.

After quadrature demodulation and reformatting according to an equivalent Pulse Repetition Interval (PRI), for each considered transmitter the surveillance channel signal can be compressed by a correlation with a noise-free replica of the reference signal, which can be regenerated according to the tracked direct signal parameters [5]. The data in the range&slow-time (r, t) domain are then provided in input to the multi-satellite processing chain.

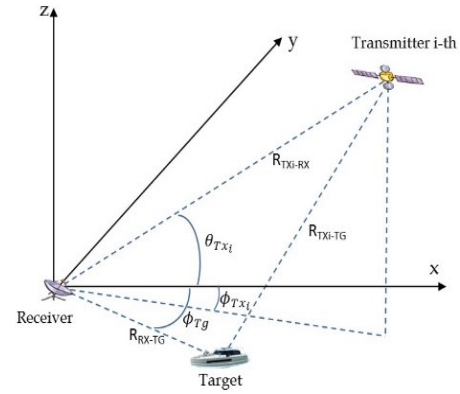

Fig. 1. Acquisition geometry.

B. Multi-satellite ship target detection technique

The main steps of the technique proposed in [11] are here briefly summarized. Particularly the technique, working in the range-Doppler (RD) domain and performing the integration on long time intervals and on multiple transmitters, comprises four steps:

1. Sequence of RD maps formation – The range compressed data pertaining to each transmitter is segmented in N_b consecutive batches of limited time duration T_b such that constant reflectivity and negligible range and Doppler migration can be assumed. A FFT in the slow-time dimension is applied to each batch to obtain a sequence of N_b RD maps.

2. Target Motion Compensation (TMC) – TMC compensates the range and Doppler migration of the target in the sequence of the N_b RD maps to allow the integration of the target returns of the entire dwell time, [6]. This is done separately for each baseline. At the output of this step all the target returns in the N_b RD maps pertaining the i-th baseline are aligned on the same position (r_i^0, f_i^0) that is the position the target occupies at t = 0. Such compensation is driven by the target Doppler rate $\dot{f}_d$, assumed constant during the dwell time.

3. Multistatic compensation – The aim of this step is to align the target contributions concerning the different transmitters to the same range-Doppler position to allow a proper integration. After this step the target is located at range bin corresponding to R_{Tg-Rx} and at Doppler bin corresponding to $-\frac{1}{\lambda}\dot{R}_{Tg-Rx}$. Such procedure is driven by the target DOA ϕ_{Tg} and its derivative $\dot{\phi}_{Tg}$.

4. RD maps integration – After the multistatic compensation procedure, the target is located in the same position in all the maps so that its returns can be properly integrated on a pixel basis.

The procedure described above depends on the specific target Doppler rate $\dot{f}_d$ (the same value can be assumed for all the baselines), on the angle of arrival ϕ_{Tg} and on its derivative $\dot{\phi}_{Tg}$. A completely adaptive technique is obtained by considering a

bank structure with different values of the above parameters. Particularly up to the second step only adaptation to the Doppler rate is required, while the last two steps of the multistatic compensation depend also on the angular values. The parameters of the best fitting branch of the bank provide also a direct estimate of the target cross-range velocity component and direction of arrival, thus enabling joint detection and localization.

III. EXPERIMENTAL RESULTS

An experimental campaign was conducted inside the H2020 SpyGLASS project, [12], focusing on Galileo signals in the frequency band E5-a. The receiver was located onto a van and placed on the shore of the river Rhine near Bonn acquiring signals reflected by different types of vessels navigating the river. Fig. 2 sketches the geometry of the acquisition. The van was also equipped with an AIS receiver to record the vessels ground truth.

In a first experiment, two passenger ferries were in the field of view of the radar and both were moving away from the receiver during a 2 mins long acquisition: 'Filia Rheni' (42m×11m) and 'Godesia' (38.6m×8.6m), of which optical photographs are shown in Fig. 3. The parameters of the experiment are listed in Table I.

Detection results obtained with the individual satellites by applying the technique in [6] are now shown. According to the analysis in [5], a batch duration of 3 sec is retained to be suitable for the considered scenario. Ten central time instants t_n={15,25,…105} have been selected, and non-coherent processing intervals around equal to $T_b \times N_b$ have been considered for N_b={1,2,6,10}. For each reference instant and number of integrated batches, the resulting RD maps (one for each considered value of the Doppler rate) feed a 2D-CA-CFAR (Cell Average Constant False Alarm Ratio) detector. Fig. 4 shows the final detection maps obtained by combining the detections corresponding to $N_b = 2$ (Fig. 4 a, c) and $N_b = 10$ (Fig 4. b, d) for sat. 1 (Fig. 4 a, b) and sat. 2 (Fig. 4 b, c). Magenta and light blue full lines represent the ground truth achieved by the AIS information for 'Godesia' and 'Filia Rheni', respectively. Probability of false alarm has been set equal to 10^{-3}. It is apparent how a number of detections form a track in good agreement with the ground truths, thus likely corresponding to the targets. Fig. 5 reports the detection results for both the targets and both the satellites for the different reference instants and number of integrated batches. From the figure, it can be observed that the detection performance progressively enhances by increasing the duration of the integration time. For example, 'Filia Rheni' has been detected in 2 over 10 cases only for sat. 1 when $N_b = 1$, whereas with $N_b = 10$ the technique provided detections for 9 over 10 cases. It is also interesting to note that while 'Godesia' is well detected by setting $N_b = 10$ with sat. 1, with sat. 2 the long integration time did not suffice to make such target detectable. The large angular diversity offered by the GNSS-based multistatic radar results in particular illumination angles where the target bistatic RCS is more or less stronger, thus resulting in better/worse situations for the target detections. It makes sense that exploiting multiple satellites can greatly help in increasing the detection performance of this system.

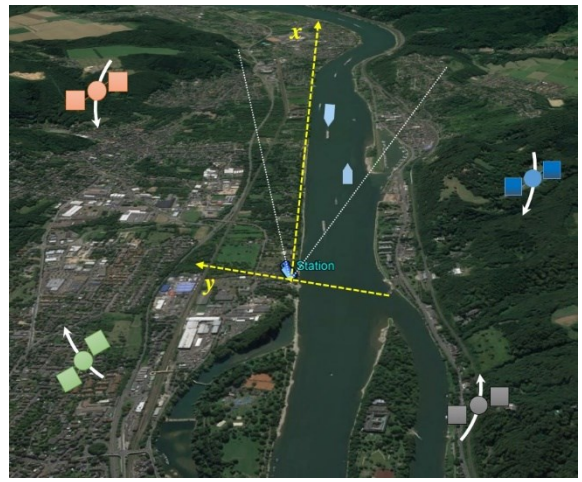

Fig. 2. Acquisition scenario.

(a) (b)

Fig. 3. Targets photographs a) 'Filia Rheni', b) 'Godesia', [13].

TABLE I. ACQUISITION 1 - EXPERIMENTAL AND SIGNAL PROCESSING PARAMETERS

Parameter		Value
Sat. 1	Number	GSAT0210
	Ranging code	PRN E01 (E5a-Q)
	Azimuth (clockwise from *x*-axis)	164.38°~163.75°
	Elevation (relevant to RX)	9.17°~9.14°
Sat. 2	Number	GSAT0214
	Ranging code	PRN E05 (E5a-Q)
	Azimuth (clockwise from *x*-axis)	-115.90°~-116.32°
	Elevation (relevant to RX)	36.02°~35.48
	Carrier frequency	1176.45 MHz
	Sampling frequency	20.46 MHz
	Dwell time	120 s
	Coherent processing interval	3 s
	Non-coherent processing interval	3-6-18-30 s

Now, the potential of the multistatic technique to both increase the detection performance and localize the target is being investigated. 'Filia Rheni', as it is the most visible with both the satellites, has been considered for the following analysis.

The difference in satellites position results in different bistatic range and Doppler histories of the targets. Fig. 6 shows the RD maps for both the satellites normalized to the mean background power ratio when t_n = 15s and for the processing parameters that will be considered hereinafter: T_b = 3s, N_b = 10, $\dot{f}_d$ providing the highest signal-to-background ratio level. By comparison with the ground truth, the bright spots visible around (1314m, -18.9Hz) in Fig. 6a (sat. 1) and around (1129m, -14.3Hz) in Fig. 6b (sat. 2), highlighted by the black boxes, likely correspond to 'Filia Rheni'. It is also worth to note that 'Godesia' is well visible in the RD map pertaining sat. 1, whereas it disappears in the second map.

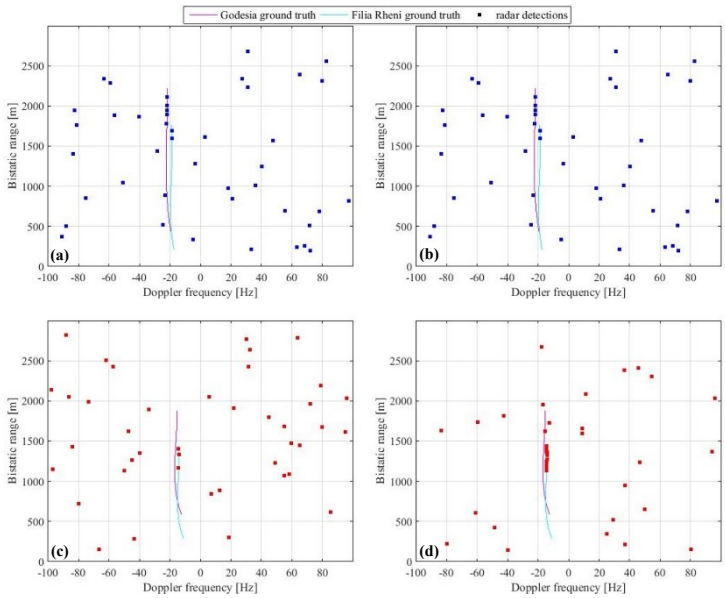

Fig. 4. Detection maps – a) sat. 1, N_b=2, b) sat.1, N_b=10, c) sat 2, N_b=2, d) sat.2, N_b=10.

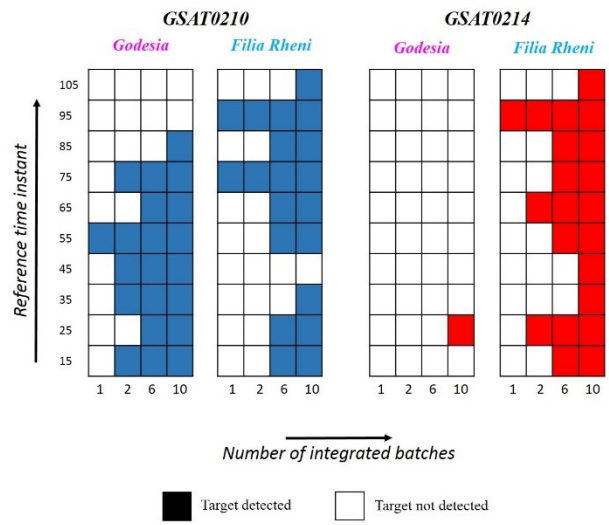

Fig. 5. Detection results.

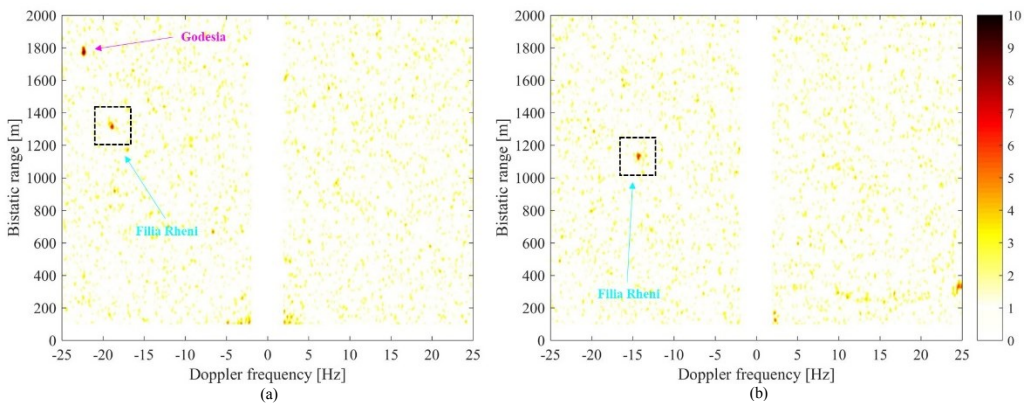

Fig. 6. Bistatic range and Doppler maps for t_n = 15s, T_b = 3, N_b = 10 – a) sat. 1 b) sat. 2.

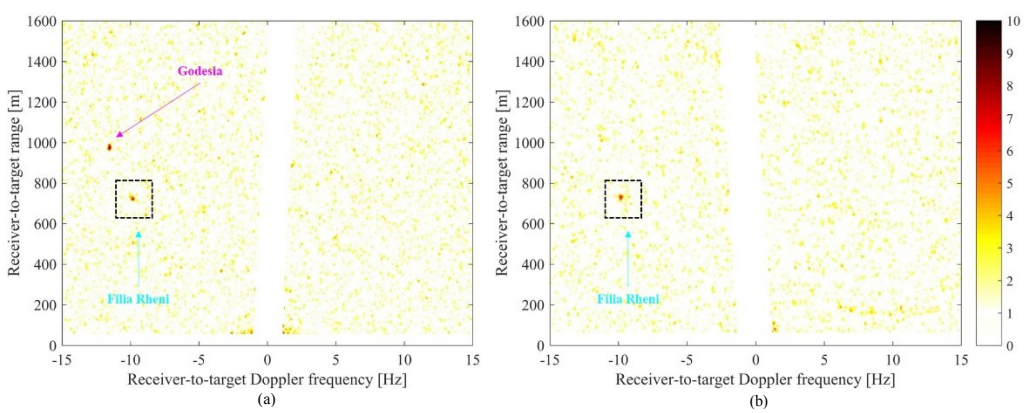

Fig. 7. Range and Doppler maps after multistatic compensation for ϕ_{TgT} = 17°, $\dot{\phi}_{TgT}$ = -0.04°/s – a) sat. 1 b) sat. 2.

The multistatic compensation step has been then applied for different values of the target DOA and its rate. Fig. 7 shows the RD maps resulting from the nominal values of the target DOA and its rate. The range and frequency axes in these images represent the range and Doppler pertaining the TG-to-RX distance. By means of the multistatic compensation, the range and Doppler position for this target, equal to (725m,-9.8Hz), is the same in both the maps, as it can be well observed by looking at Fig. 8 a and b. These figures show the patches of the RD maps containing the target normalized to the target peak power. It is worth to notice that the correspondence of the target positions in the two maps follows from the selection of the branch of ϕ_{TgT} and $\dot{\phi}_{TgT}$ banks corresponding to the actual values. When different values are exploited, the range and frequency axes are differently scaled, [11], so that the target energy will be located on different cells in the two images. As example, Fig. 8 c and d show the patches of the images pertaining the target when

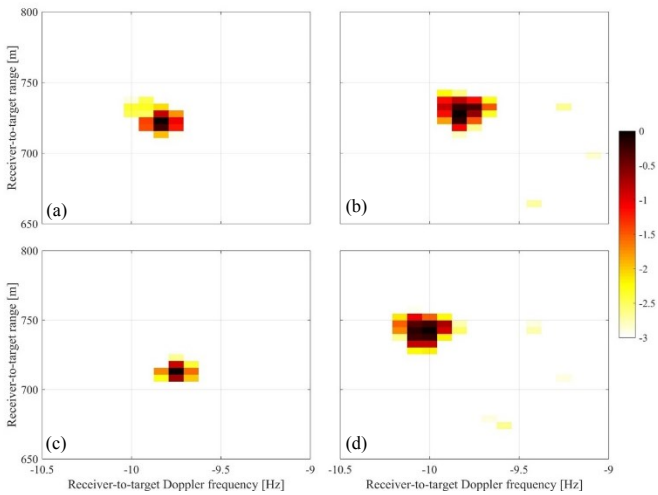

Fig. 8. 'Filia Rheni' RD maps after multistatic compensation for (sat,ϕ_{TgT}, $\dot{\phi}_{TgT}$): a) 1, 17°, -0.04°/s, b) 2, 17°,-0.04°/s, c) 1,14.5°,-0.04°/s,d) 2,14.5°,-0.04°/s

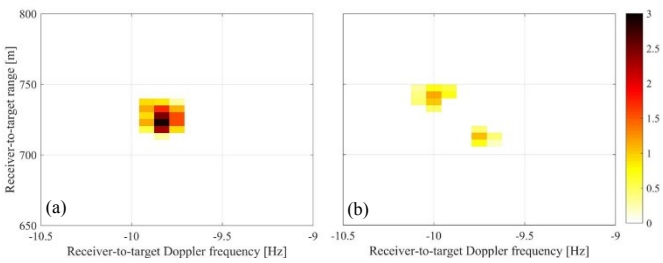

Fig. 9. Combined RD maps after multistatic compensation – a) $\phi_{TgT} = 17°$ $\dot{\phi}_{TgT} = -0.04°/s$, b) $\phi_{TgT} = 14.5°$ $\dot{\phi}_{TgT} = -0.04°/s$.

$\phi_{TgT} = 14.5°$ and $\dot{\phi}_{TgT} = -0.04°/s$. As it is apparent, in this case the target energy is differently located in the two maps.

For each tested couple (ϕ_{TgT}, $\dot{\phi}_{TgT}$), the RD images pertaining the different transmitters can be combined. Fig. 9 a,b shows the images resulting from the summation of the intensities on a pixel basis after normalization to the target peak power in the individual images for the (ϕ_{TgT}, $\dot{\phi}_{TgT}$) values considered in Fig. 8 a, b and Fig. 8 c, d, respectively. As obvious, the highest intensity has been obtained when the target energy is concentrated around the same position, namely for the actual (ϕ_{TgT}, $\dot{\phi}_{TgT}$) couple.

Fig. 10 shows the resulting multistatic integration gain (linear scale) for different values of the tested (ϕ_{TgT}, $\dot{\phi}_{TgT}$) by selecting the highest intensity obtained for the target after the multistatic compensation for t_n = 15 s. It can be seen how there is a specific couple for which the integration gain reaches the maximum, namely the number of integrated satellites. This represents the estimated DOA for the selected t_n, while the range cell providing this value represents the estimated TG-to-RX range.

By performing this procedure for each considered reference instant, the instantaneous TG-to-RX range as well as the target DOA can be retrieved and therefore transformed in Cartesian coordinate. The resulting estimated track is shown in Fig. 11 along with the one corresponding to the AIS information. It can

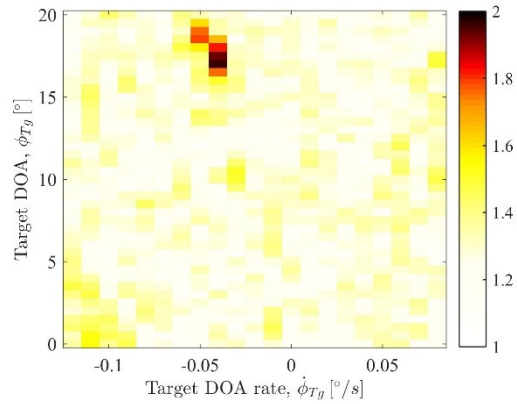

Fig. 10.Integration gain (linear scale) for t_n = 15 s.

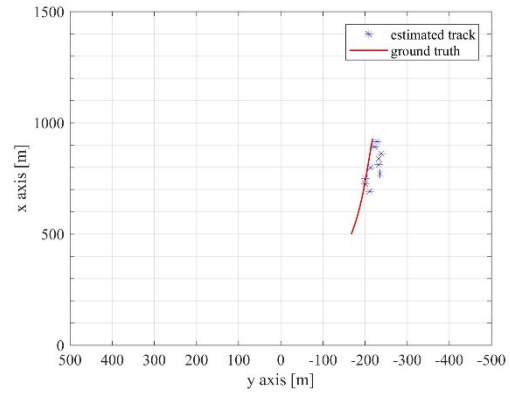

Fig. 11. 'Filia Rheni' track.

be observed the good agreement between the retrieved track and the ground truth, with a maximum difference of about 30 m and a Root Mean Square Error (RMSE) lower than 20 m.

A different target type has been considered in a second experiment: the barge 'Willem Antoine 2' (185m×11m), of which an optical photograph is shown in Fig. 12 a, was moving away from the receiver during a 1 min long acquisition. Three Galileo satellites were correctly tracked during the acquisition: GSAT0206 (PRN E30, $\phi_{TX} \approx 108°$, $\theta_{Tx} \approx 54°$), GSAT0204 (PRN E22, $\phi_{TX} \approx 79°$, $\theta_{Tx} \approx 54°$), and GSAT0211 (PRN E02, $\phi_{TX} \approx 24°$, $\theta_{Tx} \approx 40°$).

After range-compression and RD maps formation, the TMC procedure has been accomplished, considering T_b = 3s, N_b = 10, followed by the multistatic compensation step. As for the previous case study, the patches of the compensated RD maps around the target have been non-coherently integrated on a pixel basis after normalization to the target peak power for each (ϕ_{Tg}, $\dot{\phi}_{Tg}$) couple under test. Fig. 12 b shows the resulting integration gain (linear scale) for the integration window around t_n = 15s. The peak of this surface equals the number of considered TX. The corresponding couple (ϕ_{Tg}, $\dot{\phi}_{Tg}$) represents the estimated target DOA and DOA rate, while the corresponding range cell is the estimated TG-to-RX distance. Fig. 12 c shows the retrieved track compared with the ground truth provided by the recorded AIS. In this case, the RMSE between estimated and actual track is about 13 m, which is much lower than the physical dimension of the considered target.

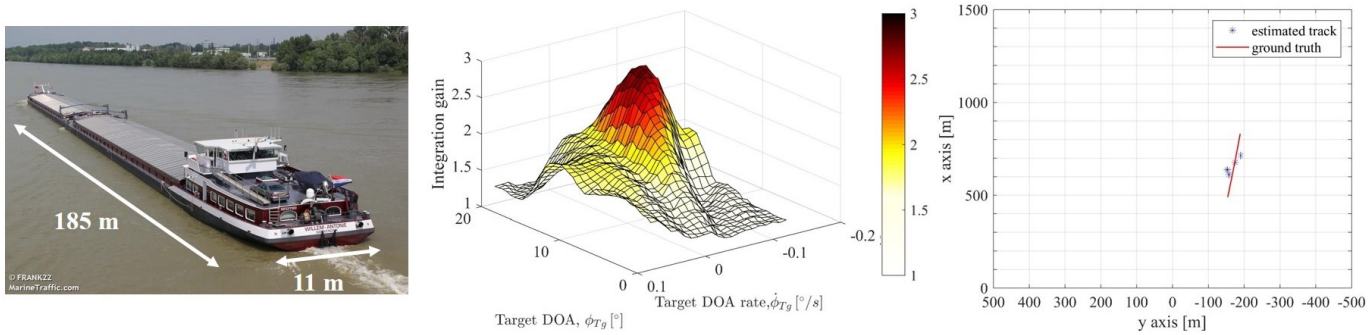

(a) (b) (c)

Fig. 12. Experiment with 'Willem Antoine 2' – a) Target photograph, [13], b) integration gain (linear scale) for t_n = 15s, c) target track.

IV. Final Remarks and Conclusions

This paper provided an experimental validation of long integration time maritime MTI technique for GNSS-based multistatic radar. The presented results have shown how the integration over long dwells at the individual bistatic level and the integration over the multiple transmitters' space can enable the joint detection and localization of ship targets of different types.

With respect to the carried out work, some final remarks are in order:

i) The unweighted summation of the bistatic RD maps might not be the optimum solution to increase the detection performance of the system. The presented work focused on a target visible in the bistatic maps after the integration over the long dwell only, and the normalization of the maps to its peak power had an illustrative purpose only. Finding the best rule to combine the multiple images is an open issue, which solution will require deeper analyses at both theoretical and experimental level.

ii) With respect to the multilateration approaches [10] that combine the bistatic ranges, the proposed method exploits the Doppler difference between the bistatic links to estimate the target range and DOA and, as further result, the DOA rate.

iii) The target localization has been performed considering one target only. As well known, in multistatic radar ambiguities may arise in the case of multiple targets: the ghost phenomenon must be considered in the future.

iv) Because the individual RD maps are combined in the power domain, the signal to background ratio improves approximately as the square root of the number of considered satellites (assuming the same signal power to disturbance level in the bistatic maps). Obviously, this entails a limited integration gain when few satellites are considered, as in the presented case studies. However, as mentioned in the introduction, a much larger number of satellites can be available by exploiting multiple fully lunched constellations, so that the final integration gain could potentially enable the detection of much smaller targets at considerably longer ranges.

v) TMC performance may be affected by not negligible target maneuvers over successive integrated batches (as a constant $\dot{f}_d$ is assumed). The integration gain achieved by exploiting the spatial diversity could allow reducing the number of integrated batches, thus making less sensitive the TMC with respect to target accelerations.

The list above maps out a number of aspects that should be addressed in future developments of this research topic, in order to exploit fully the potential of this technology.

Acknowledgment

This project has received funding from the European GNSS Agency under the European Union's Horizon 2020 research and innovation programme under grant agreement No 641486, "GALILEO-BASED PASSIVE RADAR SYSTEM FOR MARITIME SURVEILLANCE — SpyGLASS". The authors would like to thank Aster S.p.A. for providing the synchronization output.

References

[1] M. Antoniou, M. Cherniakov, "GNSS-based bistatic SAR: a signal processing view," Eurasip J. Adv. Sign. Process. 2013, 2013:98.

[2] Q. Zhang, M. Antoniou, W. Chang, M. Cherniakov, "Spatial decorellation in GNSS-based SAR coherent change detection," IEEE Trans. Geosci. Remote Sens., vol. 53, no.1, pp. 219-228, Jan. 2015.

[3] V. Koch and R. Westphal, "New approach to a multistatic passive radar sensor for air/space defense," IEEE Mag. Aerosp. Electronic Syst., vol. 10, no. 11, pp. 24-32, Nov. 1995.

[4] I. Suberviola, I. Mayordomo, J. Mendizabal, "Experimental results of air target detection with a GPS forward scattering radar," IEEE Geosci. Remote Sens. Lett., vol. 9, no. 1, pp. 47-51, Jan. 2012.

[5] H. Ma, M. Antoniou, D. Pastina, *et al*., "Maritime moving target indication using GNSS-based bistatic radar," IEEE Trans. Aerosp. Electronic Syst., vol. 54, no. 1, pp. 115-130, Feb. 2018.

[6] F. Pieralice, F. Santi, D. Pastina, *et al*., "GNSS-based passive radar for maritime surveillance: long integration time MTI technique," IEEE RadarConf 2017, Seattle, USA, May 2017.

[7] F. Santi, D. Pastina, M. Bucciarelli, "Maritime moving target detection technique for passive bistatic radar with GNSS transmitters," IRS 2017, Prague, CZ, Jun. 2017.

[8] F. Santi, M. Antoniou, D. Pastina, "Point spread function analysis for GNSS-based multistatic SAR," IEEE Geosci. Remote Sens. Lett., vol. 12, no. 2, pp. 304-308, 2015.

[9] H. Ma, D. Tzagkas, M. Antoniou, M. Cherniakov, "Maritime moving target indication and localisation with GNSS-based multistatic radar: experimental proof of concept," IRS 2017, Prague, CZ, Jun. 2017.

[10] M. Malanowski, and K. Kulpa, "Two methods for target localization in multistatic passive radar," IEEE Trans. Aerosp. Electronic Syst., vol. 48, no. 1, pp. 572-580, 2012

[11] F. Pieralice, D. Pastina, F. Santi, M. Bucciarelli, "Multi-transmitter target detection technique with GNSS-based passive radar," International Conference on Radar Systems, Belfast, U.K., Oct. 2017.

[12] http://www.spyglassproject.eu

[13] http://www.marinetraffic.com